



Meshfree simulations of spall fracture

Bo Ren^{a,b}, Shaofan Li^{a,c,*}, Jing Qian^a, Xiaowei Zeng^a

^aDepartment of Civil and Environmental Engineering, University of California, Berkeley, CA94720, USA

^bSchool of Hydro-power and Information Engineering, Huazhong University of Science and Technology, Wuhan, China

^cSchool of Civil Engineering and Mechanics, Huazhong University of Science and Technology, Wuhan, China

ARTICLE INFO

Article history:

Received 9 April 2010

Received in revised form 3 October 2010

Accepted 5 October 2010

Available online 21 October 2010

Keywords:

Ductile fracture

Meshfree method

Spall fracture

Void nucleation and growth

ABSTRACT

Shock wave induced spall fracture is a complex multiscale phenomenon, and it is a challenge to build a constitutive and computational model that can capture essential features of the spall fracture. In this work, we present a computational micro-mechanics model to simulate spall fracture by utilizing the multiscale micro-mechanics theory proposed by Wright and Ramesh [36] and a RKPM meshfree method. The focus of this work is to develop and demonstrate a simulation tool that is capable of simulations of spall fracture in engineering application. First, based on a well-known empirical formula, we relate the macroscale spall strength to the kinematics of micro void growth in a Representative Volume Element (RVE). The connection between micro void growth and overall kinematics of the RVE is made through the conservation of mass in the micro to macro transition process. Second, we develop a set of meshfree void growth algorithms that is tailored to represent kinematics of void nucleation, growth and coalescence, and these algorithms retain the conservation of mass, momentum, and energy during simulations of ductile spall fracture. Third, based on the Johnson–Cook model, we developed a meshfree computational formulation, and we have carried out simulations of the spall fracture of a Ti–6Al plate under impact loads to validate the model. From the simulation, we find that the interaction between the first two inelastic wave pulses plays an important role in the mechanism of spall fracture. The numerical results show that the proposed method can capture some features of the spall fracture, and it may be used to simulate the spall fracture in engineering applications.

© 2010 Elsevier B.V. All rights reserved.

1. Introduction

The spall fracture is a shock wave induced dynamic fracture phenomenon, which is practically important in high speed impact problems in many applications such as structures under ballistic or blast loads. The experimental results show that the macroscopic spall damage is strongly depend on material micro-structures at the length scale of (0.1 ~ 10 μm). At this specific length level, the solid is characterized by crystal grains, heterogeneous impurities, material defects and so on. Along the shock wave passage, the microscopic voids will be nucleated first, and they then grow at dislocation sites. These growing microscopic voids expand into cavities, and coalesce each others, finally they form macroscopic spall fracture cracks.

After the first observation of spall phenomena by Hopkinson [12], many experiments have been conducted to explore the mechanism of spall fracture under the shock wave loading condition. Interested readers may consult a recent monograph by Antoun

et al. [2], which has a complete survey on most of the previous work on spall fracture. In the last decade, the new experimental techniques, such as the line-VISAR [34,35] are adopted to investigate the spall fracture at mesoscale and in microsecond time duration. So far, the experimental method still cannot precisely record the dynamical process of spall fracture inside solids. Most data measured from experiments are the free-surface velocity and stress of specimen, and they are being examined by using the wave propagation theory to link to the spall fracture resistance of different materials under wide range of strain rates of shock wave loadings. For example, Gluzman et al. [9] investigated the strength properties of 35KH3NM steel under about 500 m/s impact. Kanel et al. [15] investigated the effect of initial temperature effects on spall strength of aluminum and magnesium materials by varying test temperature from room temperature to melting point. Vogler and Clayton [35] studied dynamical deformation and spall fracture of an extruded tungsten alloy, which is a dual phase polycrystalline metal.

Based on many experimental data, a recent survey by Kanel [16] has discussed the spall fracture mechanisms and governing factors. It concluded that the strain rate generated by the shock wave and the micro-structure of specimen plays very important roles in spall fracture.

* Corresponding author at: Department of Civil and Environmental Engineering, University of California, Berkeley, CA94720, USA.

E-mail addresses: shaofan@berkeley.edu, li@ce.berkeley.edu (S. Li).

Because the current experimental measurements cannot capture the spall phenomena directly, some attempted to develop numerical models and simulations to study the basic features of spall fracture. Essentially, the spall can be considered as the micro-scale void nucleation and growth, and they lead to macroscale fracture when microscale voids coalescence causes surface separation. The main focus of current models is to simulate the fracture process at microscale, and a main approach is so called the Nucleation-and-Growth model. Davison et al. [6] is an early example of such work. Subsequently, many work in this direction have been published, such as Rajendran et al. [28], Wang [37,38], etc. Recently, Wright and Ramesh [36] have applied the self-consistent theory of micro-mechanics to homogenize the microscale dynamics of void nucleation and growth in order to study spall fracture in ductile materials. In their work, a porous medium is represented by Representative Volume Element (RVE), the deformation of RVE can be divided into elastic and plastic parts. The macroscopic spherical stress in the material drives the response in the volume elements, thus the macroscopic pressure and the kinematics of growing microscopic voids are coupled automatically. At meso-scale (grain size), Krivtsov and Mescheryakov [17] used a coarse-grained molecular dynamics with a Lennard–Jones potential to simulate spall phenomena of a flyer-specimen system. At this scale, an alternative approach is to adopt the crystal plasticity theory and investigate the dynamic fracture of material by high strain rates. Clayton [5] and Vogler and Clayton [35] have used a cohesive finite element method and a rate-dependent crystal plasticity model to simulate dynamic spall fracture in polycrystalline solids. At macroscale, continuum mechanics theory is adopted to model the solid response, Kanel et al. [15] carried out a 1D simulation of spall fracture of aluminum and magnesium over a wide range of load duration. However, we have not found any publication of spall fracture simulation by using engineering computational method in multi-dimensional cases at macroscale level.

In fact, although extensive research has been carried out to investigate the mechanism of spall fracture, most these simulations have remained at the stage of academic research. To capture the dramatic changes and evolution of spall damage in a material, and material behaviors during the shock wave, and to accurately predict ductile failure process have remained to be challenges in computational failure mechanics.

During spall fracture process, a ductile solid will be undergoing extremely high strain rate deformation, and material failure starts to localize inside the solid at small scales, which pose serious challenges for computations. For instance, how to simulate the spall void formation in ductile materials by using finite element method (FEM). The finite element method seems not very successful in ductile fracture simulations because it is a thermodynamically irreversible process, which prohibits artificial numerical unloading that is essential in FEM remeshing. On the other hand, meshfree interpolations have flexibility to adapt computational domains with evolving topological structure without numerical unloading. Recently, there have been quite a few research works using meshfree methods to simulate fracture problem, e.g. Belytschko et al. [3,4]. Liu et al. [24] discussed the advantage of using RKPM meshfree method on simulation of large deformations, high gradients, and localization problems. Hao et al. [11] investigated the ductile fracture process involving damage evolution with a micromechanics cell model. Moreover, Hao and Liu [10] proposed a hybrid meshfree/finite element method, the moving particle finite element method, to solve high speed penetration and dynamic crack propagation problem. In particular, Li and his co-workers have developed a meshfree crack growth algorithm specifically targeting for ductile fracture simulations [19,30,31].

In this paper, we present a multi-scale constitutive formulation of spall fracture, which can estimate the spall strength from the

microscale information of an RVE, and then build the correlation between the macro/micro-scale kinematic quantities of RVE of solid. This approach is combined with a macroscale rate dependent thermo-mechanical meshfree Galerkin formulation to simulate dynamic behaviors of a material. The proposed method in this work uses the well-validated Johnson–Cook constitutive model as the macroscale constitutive relation for the testing material, and all required material constants are tested and documented engineering constants; hence, the proposed approach is valuable in prediction of the structure response by shock wave loading in practical engineering computations.

The paper is organized into six sections: in Section 2, we shall present a complete meshfree Galerkin weak formulation, meshfree interpolation, and constitutive update; in Section 3, we shall discuss the multiscale spall strength theory, and in Section 4, we shall present a meshfree algorithm of void nucleation, growth and coalescence. A numerical example of the impact simulation of a Ti–6Al alloy specimen is presented in Section 5, and it is compared with the experimental data. Possible mechanism of spall fracture is also discussed. We conclude the paper in Section 6 with a few remarks.

2. Meshfree Galerkin formulation with the Johnson–Cook model

2.1. The RKPM meshfree approximation

In recent years, several meshfree methods have been developed in computational mechanics, such as smoothed particle hydrodynamics (SPH) [26], Element-free Galerkin Belytschko [3,4], the reproducing kernel particle method (RKPM) [23], and h-p Clouds [8]. The particular mesh-free method used in this work is RKPM method. The detailed theory of RKPM method can be found in [22].

In this paper, The RKPM shape function $N_i(\mathbf{X})$ (see [22]) may be viewed as an enhanced version of the original SPH shape function. The basic ideal of RKPM is to construct a proper kernel function by ‘correcting’ the original SPH kernel function, $w(\mathbf{X} - \bar{\mathbf{X}})$, to satisfy the partition of unity condition so that the rigid body motion and linear deformation can be correctly represented. The RKPM interpolation function can be represented as:

$$\mathbf{u}^h(\mathbf{X}, t) = \int_{\Omega} \mathbf{C}(\mathbf{X}, \bar{\mathbf{X}}) w(\mathbf{X} - \bar{\mathbf{X}}) \mathbf{u}(\bar{\mathbf{X}}) d\Omega_{\bar{\mathbf{X}}}. \quad (2.1)$$

Here the original kernel function, $w(\mathbf{X} - \bar{\mathbf{X}})$, is obtained by a Cartesian product of the one-dimensional cubic spline function [22], and $\mathbf{C}(\mathbf{X}, \bar{\mathbf{X}})$ is called the Correction function:

$$\mathbf{C}(\mathbf{X}, \bar{\mathbf{X}}) = \mathbf{b}^T(\mathbf{X}) \mathbf{p}(\mathbf{X}, \bar{\mathbf{X}}). \quad (2.2)$$

In the above formulation, $\mathbf{p}(\mathbf{X}, \bar{\mathbf{X}})$ can be any complete basis functions. In this paper, we choose the first order polynomials or bi-linear polynomials as the basis function:

$$\mathbf{p}^T(\mathbf{X}, \bar{\mathbf{X}}) = [1, x - \bar{x}, y - \bar{y}, (x - \bar{x})(y - \bar{y})]. \quad (2.3)$$

Here $\mathbf{b}(\mathbf{X})$ is a coefficient vector, and it is determined by the reproducing condition [22], which will lead to the following vector equation,

$$\mathbf{b}(\mathbf{X}) = \mathbf{M}^{-1}(\mathbf{X}) \mathbf{p}(0), \quad (2.4)$$

where:

$$\mathbf{M}(\mathbf{X}) = \int_{\Omega} \mathbf{p}(\mathbf{X} - \bar{\mathbf{X}}) \mathbf{p}^T(\mathbf{X} - \bar{\mathbf{X}}) w(\mathbf{X} - \bar{\mathbf{X}}) d\Omega_{\bar{\mathbf{X}}}, \quad (2.5)$$

$$\mathbf{p}^T(0) = [1, 0, 0, 0]. \quad (2.6)$$

Assume that in the domain Ω there is a valid particle distribution by np particles. The RKPM kernel function is compact supported,

finally, the kernel integration, Eq. (2.1), can be discretized to form a numerical interpolation:

$$\mathbf{u}^h(\mathbf{X}, t) = \sum_{I=1}^{np} \mathbf{C}(\mathbf{X}, \bar{\mathbf{X}}) w(\mathbf{X} - \bar{\mathbf{X}}) \mathbf{U}_I(t) \Delta V_I \quad (2.7)$$

$$= \sum_{I=1}^{np} N_I(\mathbf{X}) \mathbf{U}_I(t), \quad (2.8)$$

where ΔV_I is integration weight and finally, the RKPM interpolation function is then defined as:

$$N_I(\mathbf{X}) = \mathbf{C}(\mathbf{X}, \bar{\mathbf{X}}) w(\mathbf{X} - \bar{\mathbf{X}}) \Delta V_I. \quad (2.9)$$

2.2. An explicit thermo-mechanical meshfree formulation

The high-speed impact process will produce enormous plastic deformation, and in turn the material plastic flow will generate a large amount of heat at some local area. At the locations of some material points, the temperature can sharply increase up close to melting temperature. During the spall fracture process, Kanel et al. [15] have found a large range of peak pressure in shock wave when the initial temperature of aluminum and magnesium specimen varies from room temperature to that close to the melting point. Therefore the effects of thermo-mechanical coupling and heat conduction cannot be neglected in high-speed impact simulations. In this work, a fully coupled thermo-mechanical impact problem with inelastic damage evolution is considered. By the virtual work principle, the weak formulation of equation of motion can be written as:

$$\int_{\Omega_0} \mathbf{P} : \delta \mathbf{F} d\Omega = \int_{\Gamma_0^t} \mathbf{T} \cdot \delta \mathbf{u} dS - \int_{\Omega_0} \rho_0 \frac{\partial^2 \mathbf{u}}{\partial t^2} \cdot \delta \mathbf{u} d\Omega, \quad (2.10)$$

where \mathbf{P} denotes the nominal stress, which is the transpose of the first Piola–Kirchhoff stress, and it can be related to the Kirchhoff stress as $\boldsymbol{\tau} = \mathbf{P}\mathbf{F}^T$; and Γ_0^t denotes the traction boundary where the traction force \mathbf{T} is prescribed. The above weak form formulation is obtained by integration by parts of the balance equation of linear momentums. Considering the heat generation and conduction process, the strong form of energy equation can be written as:

$$\rho_0 c_p \frac{\partial T}{\partial t} = \chi \boldsymbol{\tau} : \mathbf{d}^p + \nabla_x (\mathbf{J} \mathbf{F}^{-1} \cdot \mathbf{K} \cdot \mathbf{F}^{-T} \cdot \nabla_x T), \quad \forall \mathbf{X} \in \Omega_0, \quad (2.11)$$

where T is the temperature, χ denotes the fraction of plastic work converting to heat, ∇_x is the gradient operator in reference configuration, c_p is specific heat. For isotropic heat conduction, the heat conductivity tensor $\mathbf{K} = \kappa \mathbb{1}$, where κ is the conductivity coefficient, and \mathbf{d}^p is the plastic rate of deformation.

In general, the simulation of such coupled thermo-mechanical problem is a complex and difficult process. An effective integration scheme to solve such coupled thermal–mechanical equations is the so-called operator splitting method proposed by Armero and Simo [1]. In their scheme, a fractional time step method is adopted that is associated with an operator split of a fully nonlinear thermal–mechanical system into an adiabatic heat generation phase, followed by a heat conduction phase at the fixed configuration. Following the same procedure, the strong form energy balance equation may be also divided into the heat generation part and the heat conduction part,

$$\rho_0 c_p \frac{\partial T}{\partial t} = \chi \boldsymbol{\tau} : \mathbf{d}^p \quad (2.12)$$

and

$$\rho_0 c_p \frac{\partial T}{\partial t} = \nabla_x (\mathbf{J} \mathbf{F}^{-1} \cdot \mathbf{K} \cdot \mathbf{F}^{-T} \cdot \nabla_x T). \quad (2.13)$$

For adiabatic heating, the least square weighted residual equation is:

$$\int_{\Omega_0} \rho_0 c_p \frac{\partial T}{\partial t} \delta T d\Omega = \int_{\Omega_0} \chi \boldsymbol{\tau} : \mathbf{d}^p \delta T d\Omega. \quad (2.14)$$

In this work, the material modeling is accomplished by adopting a thermal–mechanical coupled Johnson–Cook model. For this model, we can show that:

$$\chi \boldsymbol{\tau} : \mathbf{d}^p \approx \chi \bar{\tau} \cdot \dot{\boldsymbol{\varepsilon}} \quad \forall \mathbf{x} \in \Omega(t). \quad (2.15)$$

The weak form of heat conduction equation is:

$$\int_{\Omega_0} \rho_0 c_p \frac{\partial T}{\partial t} \delta T d\Omega = \int_{\partial\Omega_0} \mathbf{J}(\mathbf{F}^{-1} \cdot \mathbf{K} \cdot \mathbf{F}^{-T} \nabla_x T) \cdot \mathbf{N} \delta T dS - \int_{\Omega_0} \mathbf{J}(\mathbf{F}^{-1} \cdot \mathbf{K} \cdot \mathbf{F}^{-T} \nabla_x T) \nabla_x (\delta T) d\Omega. \quad (2.16)$$

The first term of the right-hand side of above equation is the boundary heat dissipation. Because the response time for high speed impact/penetration only last for a few milliseconds; and normally most of the heat generated inside solid does not have enough time to dissipate into the ambient environment. For simplicity, we may ignore the part of heat that dissipates into the surrounding environment. Hence, the weak form of heat conduction equation becomes:

$$\int_{\Omega_0} \rho_0 c_p \frac{\partial T}{\partial t} \delta T d\Omega = - \int_{\Omega_0} (\mathbf{J} \mathbf{F}^{-1} \cdot \mathbf{K} \cdot \mathbf{F}^{-T} \nabla_x T) \nabla_x (\delta T) d\Omega. \quad (2.17)$$

Finally, the energy balance equation including heat generation and conduction becomes

$$\int_{\Omega_0} \rho_0 c_p \frac{\partial T}{\partial t} \delta T d\Omega = \int_{\Omega_0} \chi \bar{\tau} \dot{\boldsymbol{\varepsilon}} \delta T d\Omega - \int_{\Omega_0} (\mathbf{J} \mathbf{F}^{-1} \cdot \mathbf{K} \cdot \mathbf{F}^{-T} \nabla_x T) \nabla_x (\delta T) d\Omega. \quad (2.18)$$

Here the weak forms of balance of linear momentum, heat generation, and heat conduction are expressed in Eqs. (2.10) and (2.18).

The corresponding boundary conditions in referential configuration are,

$$\mathbf{P} \cdot \mathbf{N} = T^0, \quad \forall \mathbf{X} \in \Gamma_t, \quad (2.19)$$

$$\mathbf{u} = \bar{\mathbf{u}}, \quad \forall \mathbf{X} \in \Gamma_u, \quad (2.20)$$

here, Γ_t and Γ_u denote the traction boundary and essential boundary, and \mathbf{N} is the unit normal vector of Γ_t .

It should be noted that the meshfree interpolation used here is not able to represent essential boundary data via boundary value interpolation. Therefore, an extra term appears in the weak form Eq. (2.10)

$$\int_{\Gamma_u} T^0 \cdot \delta \mathbf{u} d\Gamma_x \quad (2.21)$$

because $\delta \mathbf{u} \neq \mathbf{0}$, $\forall \mathbf{X} \in \Gamma_u$. On how to estimate this term and enforce the essential boundary condition for meshfree methods, the readers are referred to Li and Liu [22].

By meshfree discretization, the temperature field may be interpolated by a temperature array of all particles:

$$\mathcal{T}(t) = \{T_1, T_2, \dots, T_{np}\}^T. \quad (2.22)$$

The displacement and temperature fields can be approximated by the meshfree interpolation,

$$\mathbf{u}^h(\mathbf{X}, t) = \sum_{I=1}^{np} N_I(\mathbf{X}) \mathbf{U}_I(t), \quad \text{with } \mathbf{U}_I(t) = \{U_{I1}, U_{I2}, U_{I3}\}^T, \quad (2.23)$$

$$\delta \mathbf{u}^h(\mathbf{X}, t) = \sum_{I=1}^{np} N_I(\mathbf{X}) \delta \mathbf{U}_I(t), \quad (2.24)$$

$$T^h(\mathbf{X}, t) = \sum_{I=1}^{np} N_I(\mathbf{X}) T_I(t), \quad (2.25)$$

$$\delta T^h(\mathbf{X}, t) = \sum_{I=1}^{np} N_I(\mathbf{X}) \delta T_I(t). \quad (2.26)$$

The weak form Eq. (2.10) will then become a set of discrete dynamics equations:

$$\mathbf{M} \frac{d^2 \mathbf{u}}{dt^2} = \mathbf{f}^{\text{ext}} - \mathbf{f}^{\text{int}}. \quad (2.27)$$

The conventional row-sum lumped mass matrix \mathbf{M} is adopted for explicit time integration scheme, and the external and internal force arrays are calculated as follows,

$$\mathbf{f}_I^{\text{ext}} = \int_{\Gamma_T} T_i(X, t) N_I \mathbf{E}_i dS, \quad (2.28)$$

$$\mathbf{f}_I^{\text{int}} = \int_{\Gamma_x} P_{ij}^h \frac{\partial N_I}{\partial X_j} \mathbf{E}_i d\Omega, \quad (2.29)$$

where \mathbf{E}_i is the unit vector of referential coordinate.

Then the energy balance Eq. (2.18) becomes

$$\mathbf{C}_p \cdot \dot{\mathcal{T}} = \mathbf{G} - \mathbf{H} \cdot \mathcal{T}, \quad (2.30)$$

where \mathbf{C}_p is defined as the specific thermal mass, \mathbf{G} , is the matrix related to heat generation due to plastic strain, \mathbf{H} is the matrix related to heat conductivity:

$$\mathbf{C}_p = [C_{pIJ}], \quad C_{pIJ} := \int_{\Omega_X} \rho_0 C_p N_I(\mathbf{X}) N_J(\mathbf{X}) d\Omega_X, \quad (2.31)$$

$$\mathbf{G} = [G_I], \quad G_I := \int_{\Omega_X} \chi \bar{\tau} \dot{\epsilon} N_I(\mathbf{X}) d\Omega_X, \quad (2.32)$$

$$\mathbf{H} = [H_{ij}], \quad H_{ij} := \int_{\Omega_X} \kappa F_{il}^{-1}(\mathbf{X}) F_{jl}^{-T}(\mathbf{X}) N_{i,j}(\mathbf{X}) N_{j,l}(\mathbf{X}) d\Omega_X, \quad (2.33)$$

where Ω_X is the integration weight for each particle in the background grid.

2.3. Constitutive update

During high speed impact, the propagation of shock wave induces high strain rate plastic deformation, and most of the plastic work will convert to heat [33], and consequently it leads to material softening. Hence, the mechanical response of material is a rate-dependent thermal–mechanical phenomenon.

For ductile fracture problem, the total deformation may be decomposed to three parts: elastic, plastic, and thermal parts:

$$\mathbf{d} = \mathbf{d}^e + \mathbf{d}^p + \mathbf{d}^T. \quad (2.34)$$

A rate form constitutive equation is used:

$$\overset{\nabla}{\boldsymbol{\tau}} = \mathbf{C} : \mathbf{d}^e = \mathbf{C} : (\mathbf{d} - \mathbf{d}^p - \mathbf{d}^T). \quad (2.35)$$

In the case of isotropic hardening:

$$\mathbf{d}^p = \dot{\epsilon} \hat{\mathbf{n}}, \quad (2.36)$$

where $\hat{\mathbf{n}}$ is the normal of deviatoric stress:

$$\hat{\mathbf{n}} = \frac{3}{2\bar{\tau}} \mathbf{s}. \quad (2.37)$$

In adiabatic heating, the rate of deformation induced by thermal effect is

$$\mathbf{d}^T = \alpha \dot{T} \mathbb{1}, \quad (2.38)$$

where α is the coefficient of thermal expansion, and $\mathbb{1}$ is the second order unit tensor.

Based on the Johnson–Cook model [13,14] the plastic strain rate $\dot{\epsilon}$ is calculated as follows,

$$\dot{\epsilon} = \dot{\epsilon}_0 \exp \left\{ \frac{1}{C} \left(\frac{\tau_Y}{g(\bar{\epsilon}, T)} - 1 \right) \right\}, \quad (2.39)$$

$$g(\bar{\epsilon}, T) = [A + B\bar{\epsilon}^n][1 - T^m], \quad \text{with } T = \frac{T - T_0}{T_m - T_0}, \quad (2.40)$$

where $\dot{\epsilon}_0$ is a referential strain rate, normally, we choose it as $1.0s^{-1}$, n and m are strain hardening and thermal softening parameters, T_0 is the room temperature, and T_m is the melting temperature.

In the explicit time integration, the basic field variables such as stresses, strains are calculated explicitly based on the information of the previous time step as computation progresses. To enhance the accuracy of the time integration, we adopt a fractional time increment scheme that evaluates the time derivatives of field variables at a time instance $t_{n+\theta}$ that is between t_n and T_{n+1} . To illustrate the procedure, we discuss the update of the Kirchhoff stress $\boldsymbol{\tau}$ from $t = t_n$ to $t = t_{n+1}$

$$\boldsymbol{\tau}_{n+1} = \boldsymbol{\tau}_n + \dot{\boldsymbol{\tau}}_\theta \Delta t, \quad (2.41)$$

where $\dot{\boldsymbol{\tau}}_\theta$ is the Kirchhoff stress at predicted step t_θ , $\theta \in [0, 1]$. Using the Jaumann rate of the Kirchhoff stress, we have,

$$\dot{\boldsymbol{\tau}}_\theta = \overset{\nabla}{\boldsymbol{\tau}}_\theta + \mathbf{w}_n \cdot \boldsymbol{\tau}_n - \boldsymbol{\tau}_n \cdot \mathbf{w}_n^T. \quad (2.42)$$

From Eq. (2.35), $\overset{\nabla}{\boldsymbol{\tau}}_\theta$ can be written as:

$$\overset{\nabla}{\boldsymbol{\tau}}_\theta = \mathbf{C} : (\mathbf{d}_\theta - \dot{\epsilon}_\theta \hat{\mathbf{n}}_\theta - \alpha \dot{T}_\theta \mathbb{1}). \quad (2.43)$$

To reduce the complexity of the computational algorithm, while computing the energy equation at each quadrature point, we first consider adiabatic heat generation:

$$\dot{T}_\theta = \frac{\chi}{\rho C_p} \bar{\tau} \dot{\epsilon}_\theta. \quad (2.44)$$

To compute the rate-dependent material responses, a modified forward Euler tangent algorithm is adopted in constitutive update process. The detailed information may be found in Peirce et al. [27] and Ren and Li [29], in which the Jaumann rate of the Kirchhoff stress (see Eq. (2.43)) can be obtained as,

$$\overset{\nabla}{\boldsymbol{\tau}}_\theta = \mathbf{C} : \mathbf{d}_\theta - \left(\frac{\dot{\epsilon}_\theta}{1 + \xi} + \frac{\xi}{(1 + \xi)H_\theta} \mathbf{P}_\theta : \mathbf{d}_\theta \right) \left(\mathbf{P}_\theta + \frac{3K\alpha\chi\bar{\tau}_\theta}{\rho C_p} \mathbf{I} \otimes \mathbf{I} \right), \quad (2.45)$$

where \mathbf{I} is the unit vector, and

$$\mathbf{P}_\theta := \mathbf{C} : \hat{\mathbf{n}}_\theta.$$

3. Multi-scale spall strength theory

3.1. A multi-scale spall strength formula

Since the fracture time under shock wave loading is comparable to the duration of load, the spall strength, i.e. the critical tensile stress just before the spall fracture initiates, may depend on the characteristics of loading waves. Over the last few decades, extensive experiments have been conducted for spall fracture. Experimental data with a number of materials over a large range of volumetric strain rate shows that an empirical power function

can describe spall strength in terms of decompression rate of loading wave (\dot{V}/V_0), see Kanel et al. [15], Antoun et al.[2],

$$\sigma^{spall} = A \left(\frac{\dot{V}}{V_0} \right)^m, \quad (3.1)$$

where A and m are material constants. \dot{V} means the rate of total volume of material at current time and V_0 is the total volume of material before deformation. Because this simple empirical formula can relate the complex spall fracture phenomena to measurable quantities during a spall fracture experiment, it has been widely used in the experimental analysis.

In the empirical formula (Eq. 3.1), we can find all the related variables are macro-scale quantities. However, spall fracture is obviously a multi-scale process, i.e. spall voids are nucleated at meso-scale, and subsequently they grow larger and coalesce to macro-scale voids and cracks inside the solid. Based on this empirical formula, in this paper, we try to find a theory to relate the macro-scale spall strength to the micro-scale features of solids.

From micro-mechanics viewpoint, the spall fracture can be considered as an overall effect of voids growth and coalescence inside material. Under the quasi-static condition, the macro-scale mechanics variables can be defined as the average value of a microscopic element. The solid with voids inside can be considered as a porous material, and its effective material behavior may be described by the average material behaviors of a Representative Volume Element (RVE), in which the hosting matrix contains a certain volume fraction of voids in its interior. A schematic illustration of an RVE containing voids is shown in Fig. 1.

In Fig. 1, the RVE is sketched as a solid sphere, and several micro voids are distributed inside the RVE. Following Wright and Ramesh [36], the center of mass of an RVE is located at $\bar{\mathbf{X}}$. For the RVE, we define its total mass as m , the total volume of RVE as V_t , the volume of solid inside RVE as V_s , and the volume of voids inside RVE as V_v . In this paper, we consider the spall damage as the effect of micro void growth inside a material particle, notate f be the void volume per unit total volume, i.e., the void fraction in porous material particle,

$$f = \frac{V_v}{V_t}. \quad (3.2)$$

For each RVE, we assume that when deformation starts, the material is perfect without defects, which means that $V_0 = V_s$ at $t = 0$, and we consider the solid as incompressible material. Then from the definition of RVE, we have:

$$\dot{V}_t = \dot{V}_s + \dot{V}_v = \dot{V}_v. \quad (3.3)$$

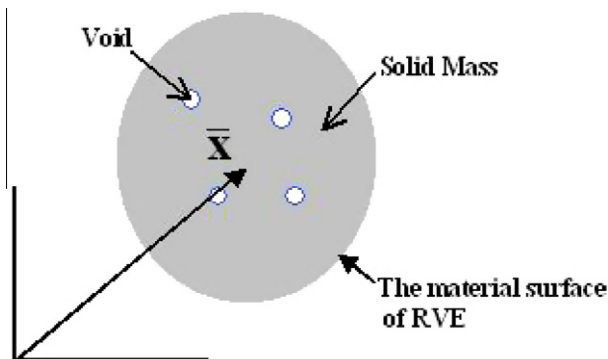


Fig. 1. The Representative Volume Element (RVE) with voids.

Then the empirical spall strength formula can be written as:

$$\sigma^{spall} = A \left(\frac{\dot{V}_v}{V_s} \right)^m. \quad (3.4)$$

The rate of void fraction can be derived as:

$$\dot{f} = \frac{\dot{V}_v}{V_s + V_v} - \frac{V_v \dot{V}_v}{(V_s + V_v)^2} = \frac{\dot{V}_v}{V_s} (1 - f)^2. \quad (3.5)$$

Finally, we can connect the spall strength to microscale quantities \dot{f} and f as follows,

$$\sigma^{spall} = A \left(\frac{\dot{f}}{(1 - f)^2} \right)^m. \quad (3.6)$$

During the spall fracture process, the spall void fraction f is cumulatively increasing. Since the spall strength can be related to the microscale quantities of a material particle, we may use the volume fraction of the voids f as the governing parameter for spall damage evolution.

3.2. The kinematics of finite deformation of RVE

Eq. (3.6) describes the relation of voids fraction and spall strength, however, f and \dot{f} are the micro features inside a material particle or an RVE, they cannot be computed explicitly in macro-scale simulation by FEM or Meshfree simulations. Back to Fig. 1, we can find that the volume of RVE is composed by solid and voids. Obviously, we have:

$$V_t = V_s + V_v \quad (3.7)$$

and let v denote the void volume per unit solid volume, then we have,

$$v = \frac{V_v}{V_s}. \quad (3.8)$$

From above definitions, we can find:

$$1 + v = (1 - f)^{-1}. \quad (3.9)$$

Now considering the conservation of mass in the porous material, we may define the average density of RVE as:

$$\bar{\rho} = \frac{1}{V_t} \int_{V_t} \rho dV = \frac{m}{V_t}, \quad (3.10)$$

where $\bar{\rho}$ is the average density of RVE. In meshfree simulation, each material particle is assigned a distinct density value. On the other hand, the average density of the solid part of RVE can be defined as:

$$\hat{\rho} = \frac{m}{V_s}. \quad (3.11)$$

From the above equations, we have:

$$\bar{\rho} = \hat{\rho}(1 - f). \quad (3.12)$$

This equation relates the macroscale mass density ($\bar{\rho}$) to microscale mass density of RVE ($\hat{\rho}$).

Then the rate of density relation should be:

$$\dot{\bar{\rho}} = (1 - f)\dot{\hat{\rho}} + \dot{f}\hat{\rho}. \quad (3.13)$$

Wright and Ramesh [36] derived macro rate of deformation of RVE from its micro properties by conservation of mass:

$$d_{ii} = -\frac{\dot{\hat{\rho}}}{\hat{\rho}} + \frac{\dot{f}}{1 - f}. \quad (3.14)$$

From Wright and Ramesh [36], when the void volume is constant, we have $\dot{\hat{\rho}}/\hat{\rho} = \dot{\bar{\rho}}/\bar{\rho}$. Therefore, they consider the first term on the right-hand side of above equation as the elastic contribution, and

the second term as the plastic contribution. For elastic deformations at the macroscopic scale, the volumetric rate of expansion may be written as the ratio of the rate of macroscopic tensile pressure \dot{p} and the macroscopic bulk modulus, hence:

$$d_{ii} = -\frac{\dot{p}}{\bar{k}(f)} + \frac{\dot{f}}{1-f}, \quad (3.15)$$

where \dot{p} is the rate of spherical stress. In this paper, it is written in terms of the volumetric rate of PK-II stress,

$$\dot{p} = \frac{1}{3} \left(\sum \dot{S}_{ii} \right). \quad (3.16)$$

As discussed in Wright and Ramesh [36], the bulk modulus of a porosity solid can be derived from the elastic properties of that homogeneous solid, the self-consistent bulk modulus of a porosity solid can be estimated as,

$$\bar{k}(f) = k \frac{4(1-f)\mu}{4\mu + 3fk}, \quad (3.17)$$

where k is the bulk modulus, and μ is the shear modulus of macroscopic material.

Finally, from above equation we can get the formula for the rate of void growth,

$$\dot{f} = 1 - f \left(d_{ii} - \frac{\dot{p}}{\bar{k}(f)} \right). \quad (3.18)$$

Note that in the above equation, except the void fraction f , the other quantities of the right side are macroscale material constants. In meshfree simulation, these constants are assign to each meshfree particles.

In this work, we assume that f is a cumulative value that starts from zero before the solid deforms. In an explicit time integration scheme, it can be calculated during constitutive update as,

$$f^{i+1} = f^i + \dot{f}^i dt, \quad (3.19)$$

where dt is time increment, and superscript i , is the time step.

In Eq. (3.18), d_{ii} denotes the trace of the macroscale rate of deformation of RVE. In this work, we assume every meshfree particle is a specific RVE with different void fraction during the damage process. Therefor, a particle or an RVE located at $\bar{\mathbf{X}}$ in reference configuration shown in Fig. 1, will move to the position $\bar{\mathbf{x}}$ in current configuration during finite deformation. This motion can be described as the velocity gradient ℓ defined in the current configuration,

$$\ell = \frac{\partial \bar{\mathbf{v}}}{\partial \bar{\mathbf{x}}}. \quad (3.20)$$

The velocity gradient can be split into two parts: a symmetric part as the rate of deformation \mathbf{d} and an anti-symmetric part as the rate of spin \mathbf{w} :

$$\ell = \mathbf{d} + \mathbf{w}, \quad (3.21)$$

$$\mathbf{d} = (\ell + \ell^T)/2, \quad (3.22)$$

$$\mathbf{w} = (\ell - \ell^T)/2. \quad (3.23)$$

In this paper, a total Lagrangian approach is adopted to represent the finite deformation of particle. Therefore, ℓ should be expressed in terms of the deformation gradient:

$$\ell = \dot{\mathbf{F}} \cdot \mathbf{F}^{-1}, \quad (3.24)$$

where $\dot{\mathbf{F}} = \frac{\partial \bar{\mathbf{v}}}{\partial \bar{\mathbf{x}}}$.

Then the rate of deformation \mathbf{d} in Eq. 3.18 can be calculated from the deformation gradient in reference configuration,

$$\mathbf{d} = (\dot{\mathbf{F}} \cdot \mathbf{F}^{-1} + \mathbf{F}^{-T} \cdot \dot{\mathbf{F}}^T)/2. \quad (3.25)$$

4. A meshfree spall nucleation and growth algorithm

4.1. Spall void nucleation algorithm

In Section 3, we have proposed a multi-scale formula to calculate the spall strength from the void fraction of each meshfree particle. At initial stage, all the macroscale meshfree particle, which is a microscale RVE, is perfect without defect; after a shock wave is sweeping through the specimen, first microscale damage occurs, and then a macroscale void may nucleate at the location of a particle when a chosen macroscale damage criterion is met.

The spall fracture is a complex process, and it is also difficult to be observed in experiments. Today, there is a general consensus that spall fracture is induced by the tensile stress generated by the compressive shock wave. In this work, we use the spherical stress of the second Piola–Kirchhoff stress (PK-II) p as the control parameter in the spall fracture criterion. When the spherical stress of a particle exceeds its spall strength, which is related to the current damage state of that particle, as indicated in Eq. (3.6), the void will nucleate at the location of this particle. However, the empirical spall strength formula Eq. (3.1) shows that spall strength will decrease with decreasing of strain rate, i.e., when the impact velocity is too low to form a shock wave, Eq. (3.1) will not be applicable. Hence, we consider the condition of spall nucleation as: (1) the tensile spherical stress of meshfree particle exceed its spall strength in Eq. (3.6), and (2) the spall strength exceed critical value:

$$p_j \geq \sigma^{spall} \quad \text{and} \quad \sigma^{spall} \geq \sigma_{cr}, \quad (4.1)$$

where p_j is the PK-II spherical stress of j th particle:

$$p_j = \left(\sum S_{ii}^j \right) / 3.0. \quad (4.2)$$

Comparing to the normal crack, a spall void is more like a cavity inside a solid, the unique shape of void makes it a real challenge to be captured in numerical calculations. In finite deformation of a ductile material, it is very difficult to construct a spall void inside a solid and re-build the current kinematic fields to keep the mass and energy conserved. However, the meshfree has inherent advantages to simulate the ductile material failure process. Simonsen and Li [30] have proposed a useful algorithm to simulate crack growth or propagation in ductile material under finite deformation. A so called parametric visibility condition algorithm is used to automatically modify the integration fields of particles without user's interference. In this paper, a modified parametric visibility condition algorithm is adopted to update the meshfree particle integration field when a void is nucleated.

For a real spall void, its potential expansion direction is the surface normal of a cave. However, the numerical simulation disperses the continuum domain with particles. To simplify this problem, we only use four particles to form a quadrangle cave to represent the spall void in 2D simulation, as shown in Fig. 2. In this paper, the meshfree particles located on the surface of voids are marked as square black boxes, the regular meshfree particles are marked as circular black dots.

Here, when the i th particle satisfies the spall criteria, Eq. (4.1), a spall void will be nucleated at the location of this particle. As shown in Fig. 2, the i th particle is split into 4 particles: i th, Numnp + 1st, Numnp + 2nd, Numnp + 3rd (Numnp is the total number of particles in the current computing domain) along the x - and y - axes separately.

The spall void is viewed as an empty cavity inside the solid shown as the shadow region in Fig. 2. In meshfree simulation, each particle is associated with a finite volume v_i , here we assume this original particle volume as the total volume of RVE, hence, the offset value of spall quadrangle δ is:

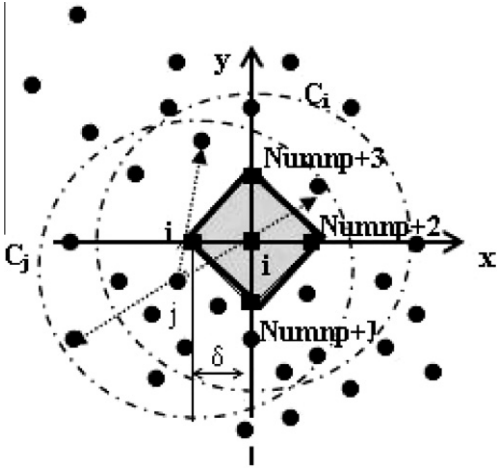


Fig. 2. Schematic illustration of void nucleation algorithm.

$$\delta = \frac{\sqrt{2}}{2} \sqrt{v_f} \quad (4.3)$$

The mass and volume of these four particles are re-assigned according to the following algorithm to keep the mass and volume conserved:

$$Mass_i^{new} = \frac{1}{4} Mass^{old} \quad i = 1, 2, 3, 4, \quad (4.4)$$

$$Volume_i^{new} = \frac{1}{4} Volume^{old} \quad i = 1, 2, 3, 4, \quad (4.5)$$

where the $Mass^{old}$ and $Volume^{old}$ are the original mass and volume assigned to i th particle before void nucleates.

The kinematic field variables, such as displacements, velocity, and accelerations of the new particles are assigned following algorithm to keep the energy conservation:

$$Disp_i^{new} = Disp^{old} + \delta \quad i = 1, 2, 3, 4, \quad (4.6)$$

$$Vel_i^{new} = Vel^{old} \quad i = 1, 2, 3, 4, \quad (4.7)$$

$$Acc_i^{new} = 0.0 \quad i = 1, 2, 3, 4. \quad (4.8)$$

The meshfree interpolation relies on a local connectivity map to associate one particle with its neighboring particles, shown as C_i and C_j for i th and j th particles in Fig. 2.

After the void is formed by these 4 particles, one has to develop a numerical algorithm that can automatically modify the local connectivity map around the void. The following parametric visibility condition is used in the simulation to modify the local meshfree connectivity map to reflect geometric change of domain due to void nucleation.

The detail of parametric visibility condition algorithm is described in Simkins and Li [21], Simonsen and Li [30]. Figuratively speaking, the spall void inside solid can be demonstrated as a specific wall-zone. A material point at one side of the wall can not “see” the material points in the other side. This principle is termed as, “visibility condition”. To determine whether or not two material points are separated by a solid discontinuous gap, one can check whether or not the line segment connecting two material points intercept that gap. However, the algorithm for line segment intercepting a spacial area (the shadow area in Fig. 2) is complex. In this paper, we only test a line segment with two diagonals of void quadrangle equivalently.

For a single spall void, one only needs to check and update interpolation fields of the nodes which located inside the supported circle shown as C_i in Fig. 2. For such a particle labeled as j th in Fig. 2, its supported circle is C_j , then one needs to test all line

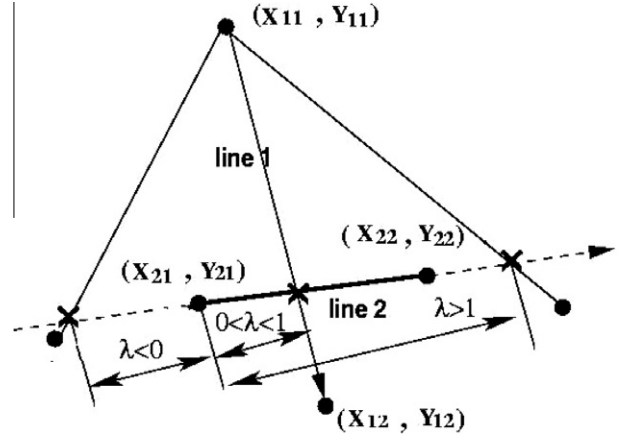


Fig. 3. The scheme of Parametric Visibility Condition.

segments which connect particle j th and its supporting particles with visibility condition.

Suppose that we want to modify connectivity relation between particle (X_{11}, Y_{11}) and the rest of particles inside C_j . We denote an arbitrary point inside C_j as (X_{12}, Y_{12}) and the vertexes of one of the diagonals as (X_{21}, Y_{21}) and (X_{22}, Y_{22}) . The parametric equations of the straight line that connects points (X_{11}, Y_{11}) and (X_{12}, Y_{12}) are:

$$X = X_{11} + \lambda_1 \Delta X_1, \quad (4.9)$$

$$Y = Y_{11} + \lambda_1 \Delta Y_1, \quad (4.10)$$

where λ_1 is the parametric variable and:

$$\Delta X_1 = X_{12} - X_{11}, \quad (4.11)$$

$$\Delta Y_1 = Y_{12} - Y_{11}. \quad (4.12)$$

On the other hand, the parametric equations for the straight line that connects two vertexes of any one diagonals of void quadrangle are:

$$X = X_{21} + \lambda_2 \Delta X_2, \quad (4.13)$$

$$Y = Y_{21} + \lambda_2 \Delta Y_2, \quad (4.14)$$

where λ_2 is the parametric variable and:

$$\Delta X_2 = X_{22} - X_{21}, \quad (4.15)$$

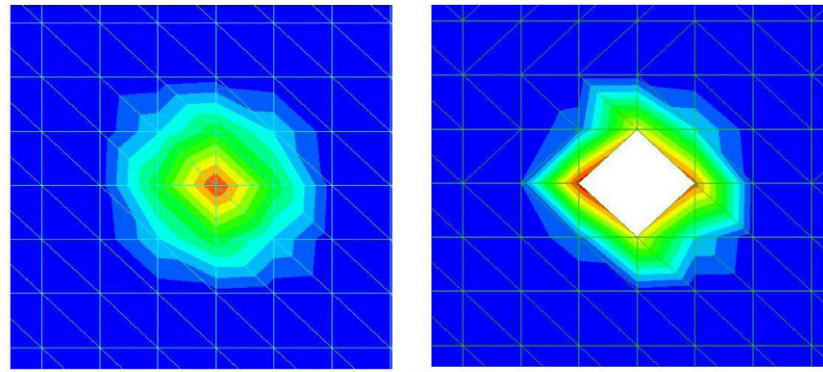
$$\Delta Y_2 = Y_{22} - Y_{21}. \quad (4.16)$$

If the two line segments intercept each other, the following Parametric Visibility Conditions have to be satisfied:

$$0 \leq \lambda_1 \leq 1 \quad \text{and} \quad 0 \leq \lambda_2 \leq 1. \quad (4.17)$$

These parametric visibility conditions are illustrated in Fig. 3. If both parametric visibility conditions are met, then the line segment between two arbitrary points inside C_j will be intercepted by the newly formed spall void, and hence one should disconnect the interpolation connections between these two points.

We can use the same algorithm to test both diagonals of spall quadrangle. If the segment (X_{11}, Y_{11}) and (X_{12}, Y_{12}) are intercepted by one of diagonal segments, one can say that segment is intercepted by that spall void. In other words, one point should be removed from the connectivity map of the other point, and it then ensures that there is no cross-void interpolation. The evolution of interpolation field of a meshfree particle by void nucleation is illustrated in Fig. 4. Fig. 4(a) shows the interpolation field of a meshfree particle (the center of high value zone), after a quadrangle cavity is nucleated, the interpolation fields of the new four particles (the four vertexes of cavity) are shown in Fig. 4(b). It can be seen that there is no interpolation field going through the cavity space, and one can say the shadow area in Fig. 2 is a physical cavity inside solid.



(a) Interpolation field of a particle. (b) Interpolation field around a void.

Fig. 4. Change of meshfree interpolation field around a nucleated void.

4.2. Void growth algorithm

Recently, Wright and Ramesh [36] utilized the average kinematics variables of an RVE to formulate a micro-mechanics based spall void growth criterion, and Vogler and Clayton [35] have applied cohesive finite element method to simulate the spall mechanism based on the different grain orientations. Nevertheless, up until today, the mechanism of spall fracture is still not very clear, besides most people agree that the spherical tensile stress inside solid is the primary factor to drive the spall growth. Therefore in this work, to carry out a macroscopic engineering simulation of spall phenomena, we simply use the spherical stress of PK-II as the main variable to estimate the spall void growth process. We assume that when the spherical stress of a particle near a vertex of a spall void exceeds a critical value, the vertex of the spall void will propagate to this specific particle. This criterion can be described by following expression:

$$p_j > p_{cr}, \tag{4.18}$$

where p_{cr} is the critical value that controls the process of spall void growth.

In reality, the potential expansion direction of a spall void is the normal direction of void surface, and the shape of the spall voids is probably a sphere in three dimensional space and a circle in two dimensional space. However, just as we use quadrangle instead of the circle shape voids to nucleate a new void, in the meshfree simulation, we simply assume that the spall void growth directions are localized at the four vertexes, and each vertex is attached to a meshfree particle. Therefore, each vertex expands in a quarter fan from the original particle position, as indicated as I, II, III, IV quadrant in Fig. 5.

Fig. 5 gives an illustration that if the vertex of quadrangle satisfies the void growth criterion, Eq. (4.18), the vertex will then propagate to another particle. For example, the vertex (particle No. Numnp + 3) propagates to particle j th inside the IV quadrant at current time step. Therefore, the current spall void shape is shown as a polygon with particles: i th, Numnp + 1-th, Numnp + 2-th, Numnp + 3-th, j -th, Numnp + 4-th. And the current spall void has four potential growth vertexes as i -th, Numnp + 1-th, Numnp + 2-th, and j th in the next time step. From Fig. 5, we can find that the old vertex is split to two particles (Numnp + 4-th and Numnp + 3-th). For each vertex, the spall growth algorithm is exactly the same as the crack propagation algorithm proposed by Simonsen and Li [30], and we use the same algorithm for crack growth, which can keep mass and energy conserved.

After carrying out the particle splitting algorithm, the connectivity of meshfree interpolation has to be updated in order to form

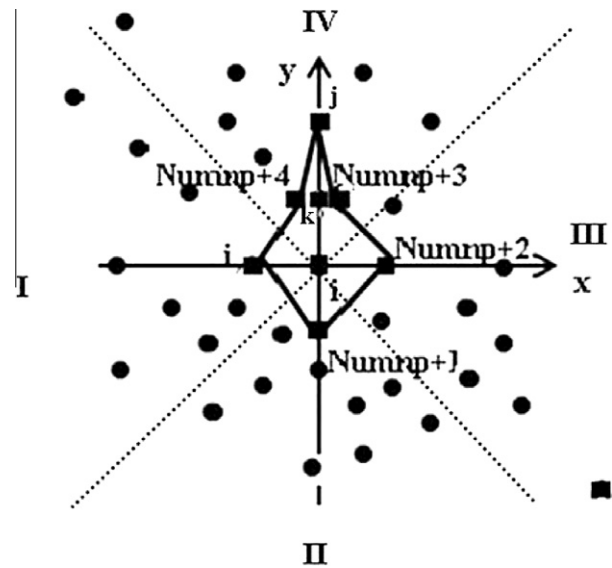


Fig. 5. Schematic illustration of void growth algorithm.

a cavity space in meshfree simulation domain. To do so, we can use the same Parametric Visibility Condition algorithm described in Section 4.1 to update interpolation field of particles near each new vertex. Comparing with the visibility condition algorithm for spall nucleation, here we only need to test the interpolation connectivity between two particles with the line segment that connect the new vertex and the middle point of new split particles shown as line segment $k - j$ in Fig. 5.

4.3. Void coalescence algorithm

In this work, the spall void growth is through the process of void coalescence. In the following, we describe a meshfree void coalescence algorithm.

We assume that when the vertex of one spall void propagates to a vertex of another spall void, these two spall voids will be coalesced to form a bigger void as shown in Fig. 6(a) and (b).

When two spall voids coalescence, the two closest vertexes, the i th and j th particles in Fig. 6(a), of spall voids will be split into two particles as shown in Fig. 6(b). The particle split algorithm is similar with the spall nucleation algorithm described in Section 4.1. The physical properties of new two particles will be assigned according to the following rules:

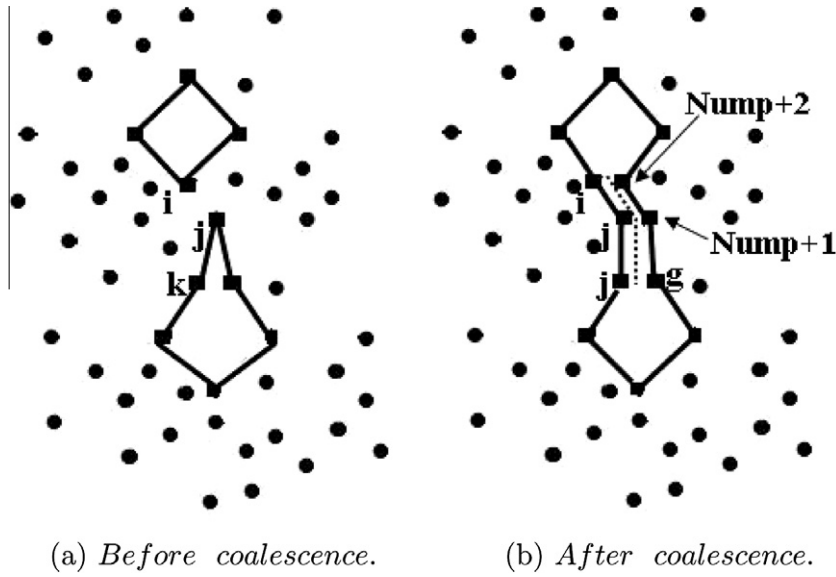


Fig. 6. The illustration of spall void coalescence algorithm.

$$Mass_i^{new} = \frac{1}{2} Mass^{old} \quad i = 1, 2, \quad (4.19)$$

$$Volume_i^{new} = \frac{1}{2} Volume^{old} \quad i = 1, 2. \quad (4.20)$$

The kinematic field variables, such as displacements, velocity, and accelerations of the two new particles are assigned as:

$$Disp_i^{new} = Disp^{old} + \delta \quad i = 1, 2, \quad (4.21)$$

$$Vel_i^{new} = Vel^{old} \quad i = 1, 2, \quad (4.22)$$

$$Acc_i^{new} = 0.0 \quad i = 1, 2. \quad (4.23)$$

After particle splitting, the two dashed line segments, which are located in the middle of new split particles in Fig. 6(b), are used to update the interpolation connectivity of the meshfree particles near the split particles by using the Parametric Visibility Condition algorithm described in Section 4.1. In this particular case, the polygon cavity in Fig. 6(b) represents a bigger spall void.

To demonstrate the meshfree void nucleation, growth and coalescence algorithm described in this section, a numerical simulation of a flyer/specimen impacting process is carried out to show how the meshfree spall fracture algorithm to capture the spall fracture phenomena qualitatively. In this example, the dimension of the target specimen is 50 mm × 7 mm; and the dimension for the flyer is 50 mm × 2 mm. In this work, the flyer is treated as a rigid body, and the target specimen is modeled as a thermo-elasto-viscoplastic solid, the detailed formulas of the constitutive model as well as the material constants are chosen exactly the same as that in Li and Simonsen [19]. In the simulation, the impact speed of the flyer is set at 80 m/s. For the spall strength formula, we choose the experimental data for stainless steel from Antoun et al. [2], which are: $A = 0.65$ GPa, $m = 0.11$; and the critical spall strength of void nucleation and critical spherical stress of void growth are simply set as: 2.4e8 GPa the same as in the literature, which will make voids coalescence easily. The simulation result is shown in Fig. 7. In the numerical example calculated, there are 237 voids nucleated over the entire process, and these voids merge together with each other at the growth phase. Finally, all these individual voids are coalesced into one macros crack. Fig. 7(b) shows that the stress is released at the crack surface, which implies that a physical surface separation is formed inside solid successfully. This case demonstrates that the proposed meshfree algorithm indeed works well.

5. Numerical simulations

5.1. Simulation model

Numerical simulations have been performed to validate the method proposed in this work. To compare with the experimental data, we choose to simulate an impact test problem that was carried out by Kanel [16]. The simulation set-up is the same as the experiment, and the specimen-flyer impact system is depicted in Fig. 8. In the experiment, the specimen material is Ti-6Al alloy, the flyer is an aluminum-alloy plate, and it was launched with velocity of 600 ± 10 m/s to impact the side edge of the specimen. To simplify the simulation problem, we set the flyer as a rigid plate, but its density is still taken the same as the aluminum-alloy plate used in the experiment. For a high speed contact-impact problem, the error induced by this simplification is under tolerance level. In this paper, we do not discuss the meshfree contact algorithm used in the simulation. The readers who are interested in the meshfree contact algorithm can consult Li et al. [20] for details. One of the main reasons for choosing Ti-6Al alloy's experimental data to compare with the simulation is because its material properties are well documented in literature.

First, Ti-6Al alloy has been carefully matched with the Johnson-Cook model by many research groups, e.g. Lee and Lin [18], Meyer and Kleponis [25], Seo et al. [32]. We choose the latest J-C material constants for Ti-6Al alloy reported by Dorogoy and Rittel [7]. This is because they used the shear compression specimen (SCS) in the experimental test to obtain material parameters. Considering the fact that the main factor that drive fracture in ductile material is shear stress, their data is more relevant to this simulation. The material constants chosen for this simulation are listed in Table 1. Second, for spall strength calculation, the material constants of Ti-6Al alloy are taken from the monograph by Antoun et al. [2], which are listed in Table 2. There is no explicit data reported in literature for the minimum critical spall strength obtained in shock wave impact experiments (see Eq. (4.1)). However, according to the log-log line about strain rate-spall strength in Antoun et al. [2] (Fig. 5.3, p. 144), we choose the minimum spall strength for Ti-6Al as 2.3e9 Pa based on linear extrapolation. Moreover, there is no experimental data reported about the critical tensile spherical stress, which governs the spall crack growth too. To obtain the critical tensile spherical stress, in this simulation, first, we simulate the impact system

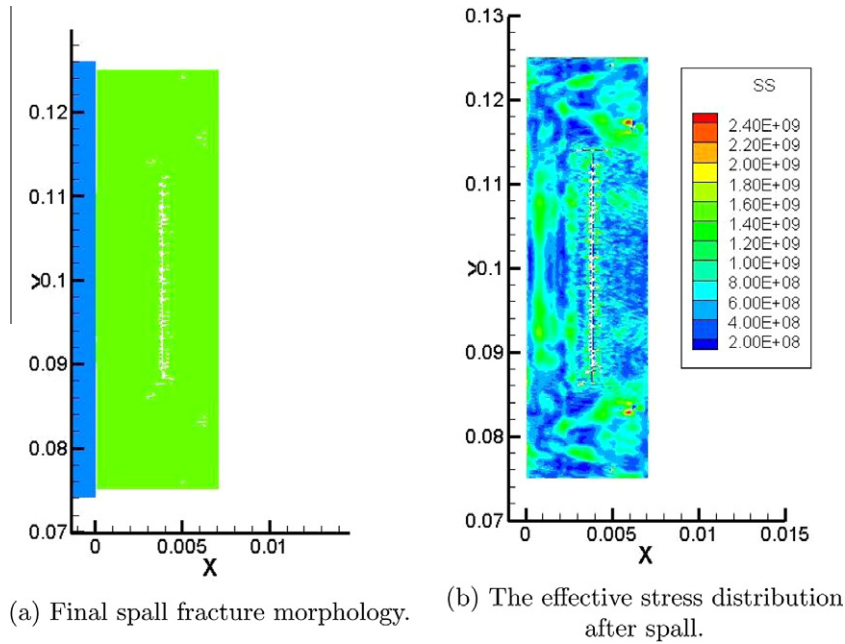


Fig. 7. A simulation of spall fracture by using meshfree void-growth algorithm.

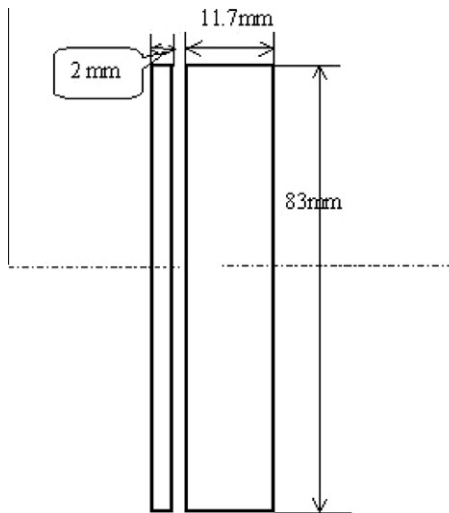


Fig. 8. The dimension of computation configuration.

Table 1
Material parameters of the Johnson-Cook model for Ti-6Al alloy.

Parameter	Value	Definition
E	113.8 GPa	Young's modulus
ν	0.342	Poisson's ratio
ρ	4430 kg m ⁻³	Mass density
A	880 MPa	Yield stress
B	695 MPa	Strain hardening
n	0.36	Strain hardening index
$\dot{\epsilon}_0$	1.0 s ⁻¹	Reference strain rate
m	0.8	Temperature softening
C_p	526 J (kg K) ⁻¹	Specific heat
α	32.0 × 10 ⁻⁶ K ⁻¹	coefficient of thermal expansion
χ	0.9	The fraction of plastic work converted to heat
k	6.7 W\m - k	Thermal conductivity
T_0	300.0 K	Room temperature
T_m	1900.0 K	Melting temperature

Table 2
Spall constants of Ti-6Al alloy.

Parameter	Value	Definition
A	0.39 GPa	Parameter1
m	0.19	Parameter2

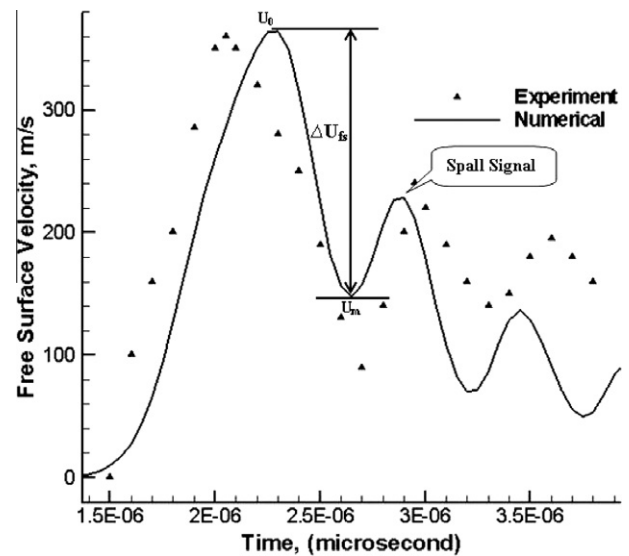


Fig. 9. Free surface velocity profile of experimental and numerical result for Ti-6Al alloy.

without spall fracture, then at the moment when the spall crack initiates under the mimic experiment condition, we measured the numerical tensile spherical stress. The spherical stress measured in numerical experiment is close to 4.0 GPa. Hence we simply choice a critical sphere stress (see Eq. (4.1)) as 4.0 GPa.

Table 3

The compare with experiment and simulation.

	U_0		U_m		ΔU_{fs}	U_p	
	Value (m/s)	Time (μ s)	Value (m/s)	Time (μ s)	value (m/s)	Value (m/s)	Time (μ s)
Experiment	360.0	2.04	77.0	2.7	283.0	240.0	2.95
Numerical	364.0	2.25	140.0	2.65	224.0	228.0	2.9

In the actual meshfree simulation, 12,000 particles are uniformly distributed in the whole computational domain. For 12,000 global meshfree interpolation functions, we have used 46,644 Lagrangian quadrature points for numerical integration. The simulation is conducted by using one blade of a SuperBlade cluster system with 8 CPU: Intel (R) Xeon (R) E5405@2.00GHZ (X8), RAM:1.5 GB. The computing response time is 5.0 μ s, the computing time is 3.35 h.

5.2. Simulation details

The current experimental approach cannot record the dynamic history of particles inside a solid at small scale. Therefore, the free-surface-velocity history at the side edge opposite to the contact surface edge is widely used to investigate the spall behavior (see [2,16]) as a means for indirect measurement. It is believed that the free surface velocity history may provide some clue for the history of the stress wave inside a solid. After the compressive stress reaches to the free surface, a tensile stress starts to propagate towards the impact side of the plate. First the free surface velocity reaches peak point (U_0) and begins to unload. When the tensile stress exceeded spall strength, spall voids begins to nucleate and accumulate in the damage zone. As the main feature of spall fracture, the damage zone is located inside material specimen, and its formation is strongly affected by the presence of the boundary, or in other words, multi-dimensional boundary effect will significantly affect shape and location of the damage zone as well as the void distribution inside the zone.

As the result of complex interaction between free surface and compressive wave pulses, a compressive disturbance called “spall signal” appears on the free surface velocity history, (see Fig. 9). In experimental approach, the ΔU_{fs} , shown in Fig. 9, is an important value to determine spall strength:

$$U_{fs} = U_0 - U_m, \quad (5.1)$$

where, U_m is the free surface velocity just before the arrival of the spall signal.

The experimental data for free surface velocity obtained from Kanel [16] and the numerical simulation result obtained from our simulation are compared in Fig. 9. Because the experiment approach cannot trace the moment of contact, we juxtapose the experimental curve and numerical curve at the time point where the compress wave reaches at free surface, i.e., the velocity begins rising. And in Fig. 9, numerical result is the velocity history of the middle point of the free surface. The main features of free surface velocity of experiment and numerical results are compared in Table 3, here U_p is the peak point of spall signal.

One may find that in the early period before spall void nucleates (the first wave), there is a small offset or phase error between the numerical and experimental wave shapes, which result in a 0.19 μ s delay of numerical U_0 , see Table 3. We think that this error may come from three sources: (a) the approximation made in the mesh-free contact algorithm used in the simulation [20]; (b) the phase error of shock wave simulation due to meshfree spatial discretization, and (c) the flyer is taken as a rigid body in numerical simulation. For ultra-high speed contact and impact problems, how to find a realistic contact force is pragmatic in the current meshfree

algorithm, and it is still a challenge to find an accurate contact force under such conditions in numerical simulations. On the other hand, all discretization based numerical methods introduce numerical pollution when simulating high frequency wave propagations. A manifestation of such numerical pollution is the phase error of the numerical solution. Thus it is highly possible that in this case the spatial particle density simply does not have enough resolution to capture the high frequency oscillation at the shock front. Last source that may introduce numerical error may be due to the rigid body modeling of the flyer. That approximation may also induce phase error in number of different ways for impact and reflection waves during the simulation. The actual error may be the combination of these three sources and their interactions.

Physically, the spall fracture is a multiscale problem, though in this work we only used the average properties of RVE to derive the macro-scale formulas for spall fractures, this approximation may lead to differences in U_{fs} between the numerical simulation and experimental measurements. From the engineering application standpoint, the results of numerical simulation and experimental measurement fit each other well at void nucleation phase, i.e. the voids nucleate at the right location and right time. During the ensuing void growing phase, the numerical results do not fit well with the experimental data. A possible reason for this is because of that in this work we do not take into account the kinematics and the dynamics effects of the void growth.

The time sequence of the numerical simulation is shown in Fig. 10. When the flyer impacts the specimen, a pulse of compression stress wave (the blue¹ region in Fig. 10(a)) is formed by the contact force. The shock wave propagates towards the free surface, and it arrives at free surface at $t = 2.1 \mu$ s (as shown in Fig. 10(b)). Then the free surface starts to unload, and a reflection tensile wave (the red region in plots) propagates back to the impact side of the specimen. That tensile stress nucleate spall fracture at $t = 2.35 \mu$ s, shown in Fig. 10(c). In this simulation, the nucleation phase goes on from 0.3 μ s to $t = 2.65 \mu$ s, as shown in Fig. 10(d) and (e). Then the spall voids begin to grow under the spherical tensile stress momentarily, the spall void growth phase begins at $t = 2.85 \mu$ s and ends at $t = 3.0 \mu$ s, as shown in Fig. 10(f) and (g). The final profile of spall fracture is shown in Fig. 10(h) at $t = 5.0 \mu$ s.

Zooming in the damage zone, we can find the spall voids are nucleated where is closed to the top and bottom sides of specimen in the first, subsequently they tend to form at the middle section of specimen, as shown in Fig. 11(a) and (b). During the spall voids growth phase, the volumes of voids increase, and they may coalesce each other to form a bigger void, a detailed morphology is shown in Fig. 11(c).

Although spall phenomena is a complex multiscale process, and it is affect by many factors ranging from loading conditions, material heterogeneity, to mesoscale microstructure such as grain boundary, all existing work in the literature point out that the tensile spherical stress is the main factor that drives spall fracture. Nevertheless, this still cannot explain when and where the spall void will start to nucleate.

¹ For interpretation of color in Fig. 10, the reader is referred to the web version of this article.

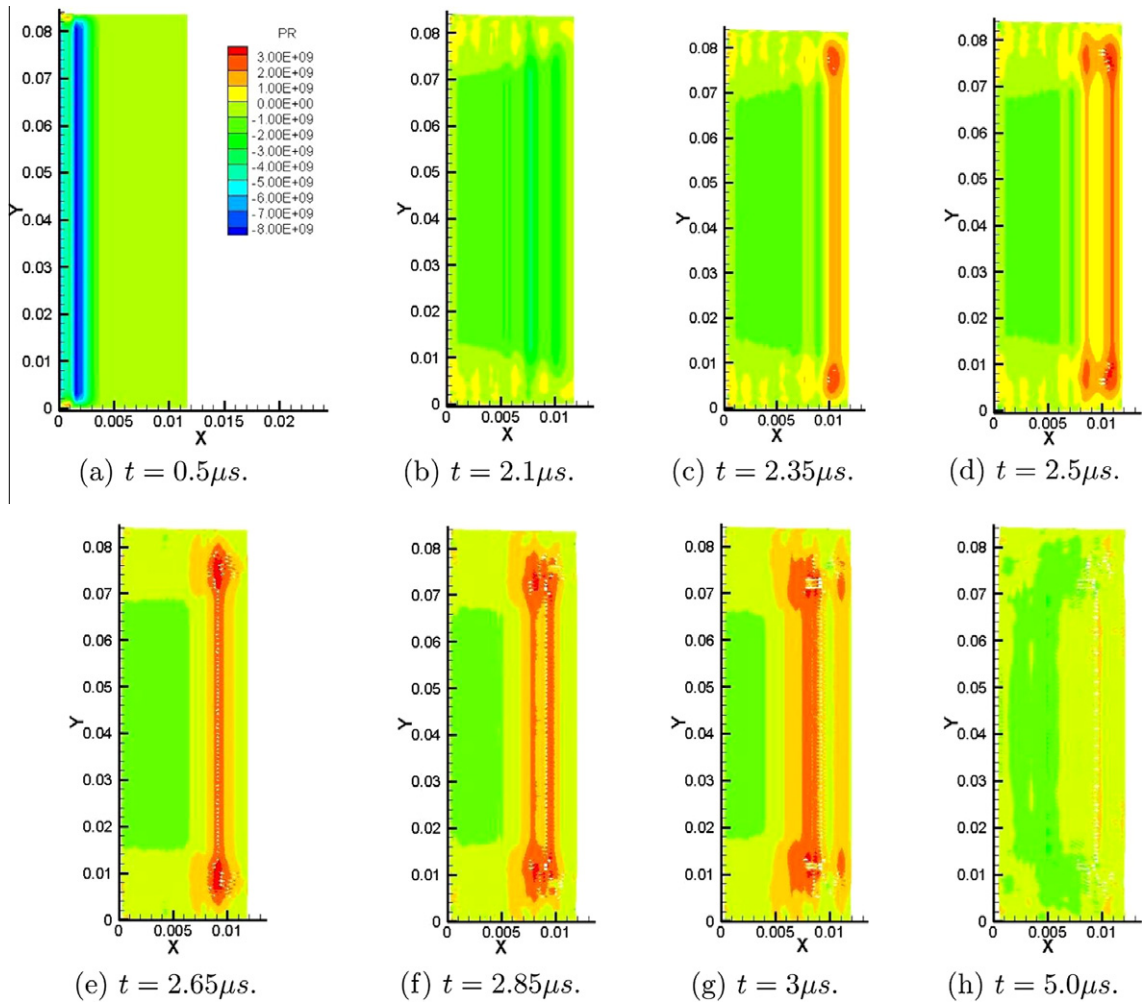


Fig. 10. The dynamics of spall fracture driven by tensile stress, shown as spherical stress.

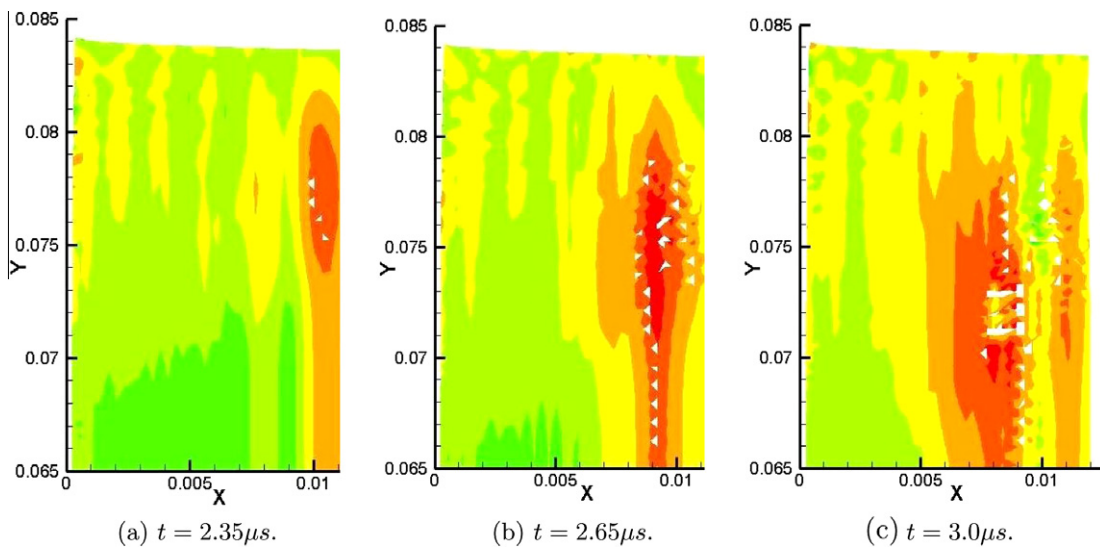


Fig. 11. Details of spall fracture morphology.

To discuss the possible mechanism of spall fracture, we measure and record the history of the spherical stress p of the second Piola–Kirchhoff stress with time at a material line located in the

middle section of the specimen along the vertical direction, as shown in Fig. 8 (the dashed line). The results of spherical stress is illustrated in Fig. 12. In Fig. 8, the contact surface is located at

horizontal position 0.0 mm, and the free surface is at horizontal position 11.2 mm. At $t = 1.1 \mu\text{s}$, Fig. 12(a), we can find there are several compressive waves (shown as wave I, II and III) inside solid, which is induced by the dynamical contact process. These compressive wave pulses propagate towards free surface. At $t = 1.7 \mu\text{s}$, Fig. 12(b), the front of wave pulse I reaches to the free surface, and it begins to reflect from free surface, with wavelength λ_1 , here, the wave pulse II has wavelength λ_2 . At $t = 2.4 \mu\text{s}$, Fig. 12(c), the front of wave pulse II reaches to the free surface, and it begins to reflect. At this time, the wave pulse I has been reflected completely, and has begun to propagate towards contact surface. Therefore, at $t = 2.5 \mu\text{s}$, Fig. 12(d), there are two tensile

wave pulses move in opposite directions. The peak values of these two tensile waves will superpose each other at $t = 2.65 \mu\text{s}$ to form a high tensile spherical stress plus, Fig. 12(e). This combined high spherical tensile stress amplitude may initiate the spall fracture inside the solid. At $t = 2.9 \mu\text{s}$, Fig. 12(f), this high tensile zone will be split by the spall voids.

So far most of the results on spall fracture are based on a postulate derived from experimental observation that the spall damage is induced by the stack of the reflected tensile wave from the free surface specimen and flyer e.g. Antoun et al. [2]. Based on our simulation results, we think that the high-speed impact of deformable objects is a transient event, and the contact time between the flyer

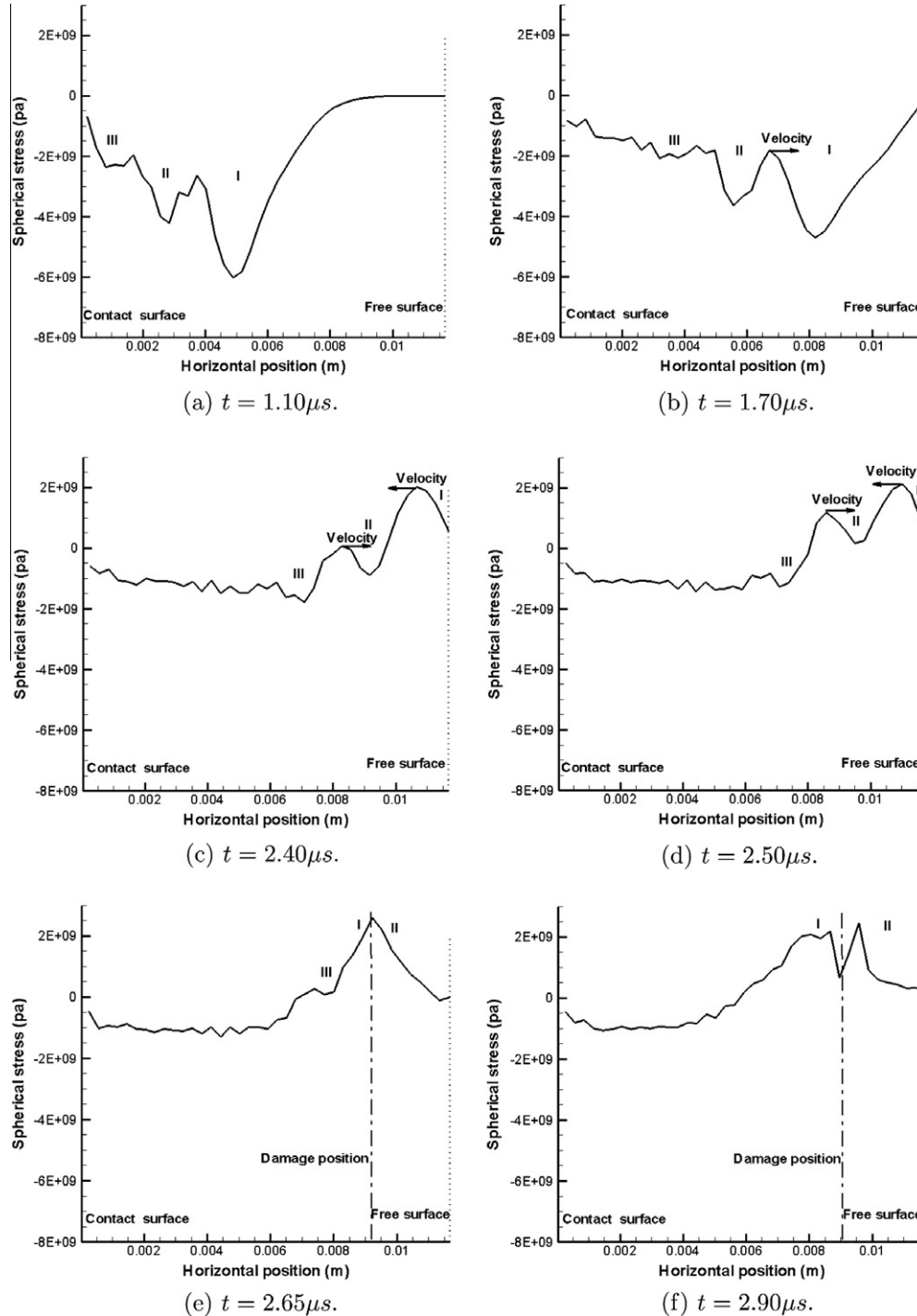


Fig. 12. The spherical stress profile inside the specimen.

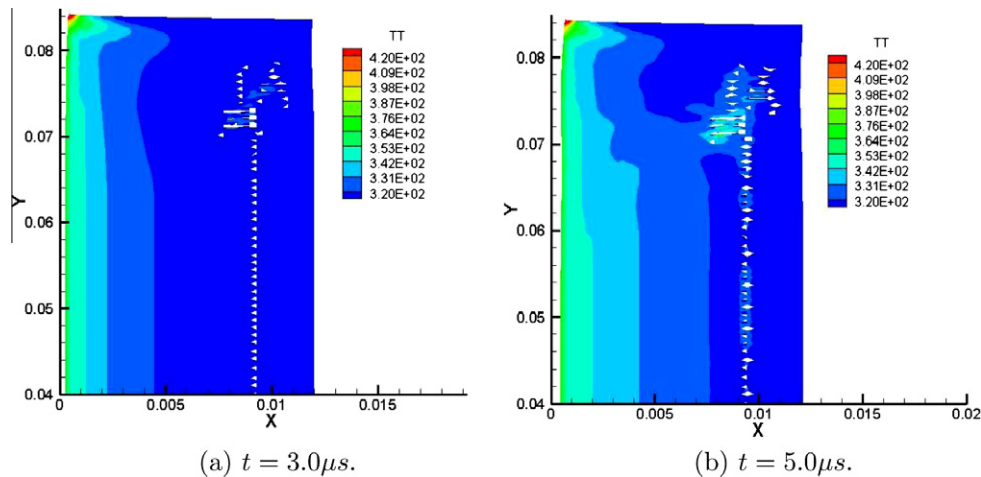


Fig. 13. The temperature distribution after spall damage.

and specimen is finite. The tensile wave from flyer may be hard to transfer through the interface between flyer and specimen. During this simulation, we find that the difference of reflection time of compressive wave I and wave II may generate a high tensile spherical stress plus inside solid. It appears that there are two positive wave pulses collide as shown in Fig. 12(e), and the combined amplitude is higher than the initial reflected wave I pulse (see Fig. 12(d)). Moreover, it appears that the spall voids nucleate at the location where these “positive wave pulses” collide. First this phenomenon indicates that the second wave pulse has been elevated into a tensile wave pulse before it even reaches to the free surface. This phenomenon may be hard to find by experimental observation because of the limitation of the current experimental technology. To the best of the authors’ knowledge, this phenomenon is first reported in numerical simulations.

We tend to believe that the elevation of the second wave pulse to a tensile wave pulse (before it reaches to the free surface) may be due to a complex interaction with the reflected first wave pulse. During this event both its amplitude and its phase may have changed during a non-linear inelastic wave collision. This sets up a stage for “two tensile wave” collision, which leads to a new high on spherical tensile stress in the solid.

In general during plastic deformation, the plastic work converts to heat that induces heat softening. The temperature profiles of the specimen are shown in Fig. 13. Fig. 13(a) shows the moment when the spall damage process nearly finished ($t = 3 \mu\text{s}$), and Fig. 13(b) shows the moment when the spall damage has finished for a while ($t = 5 \mu\text{s}$). During this period, the high temperature is mainly located at the contact surface, and there is no sharp high temperature region near the spall damage zone, which means that the plastic deformation may not affect the spall damage much, because spall fracture is a transient dynamic phenomena, and during the process, there is no large scale plastic deformation accumulated at where the spall fracture occurs.

6. Discussions

Simulation of spall fracture is a challenge in computational failure mechanics. In this work, we have presented a phenomenological two-scale micro-mechanics formulation to describe the kinematics of spall void formation and evolution, and we have developed a meshfree method to simulate spall void growth and coalescence.

Comparing with experimental data, the numerical results obtained in the simulation show that the proposed method can simulate the spall phenomena well.

To describe the complex multi-scale spall fracture, we have first developed a formula for macro spall strength, which is related to kinematic measures of micro spall void based on an empirical equation; then we built the correlation relations between the micro kinematic quantities of spall void and the macro dynamics quantities; Second, we have developed an explicit thermal-mechanical constitutive update with the Johnson–cook model for the high strain rate ductile deformation; Third, we have proposed novel meshfree algorithms of spall void nucleation, growth and coalescence in a solid. These meshfree algorithms can automatically generate cavity or spall void inside a solid based on prescribed physics criteria. Finally, a Ti–6Al flyer/specimen impact process is conducted to investigate the mechanism of spall fracture. Based on the numerical results obtained, we have found that there is a strong and complex interaction between the first two inelastic wave pulses near the free-traction surface. Such an interaction will create a collision between the peaks of the first reflected wave pulse with the elevated second in-coming wave pulse. The superposition of these two wave peaks creates a maximum tensile state that may be the mechanism for spall fracture in ductile materials.

This paper is both an original research and an on-going research to simulate the spall fracture in ductile materials. There are some other issues to remain to study, such as the mechanism of spall void expansion and how to simulate it. In the future work, a meso-scale to macroscale void growth model is to be developed in three-dimensional space in order to capture the complete multiscale features of spall fracture.

Acknowledgments

This work is supported by a grant from Army Research Laboratory to NextGen Aerospace Co., which is sub-contracted to the University of California at Berkeley. Dr. T. Wright and Dr. J.D. Clayton of Army Research Laboratory have been the technical advisors.

References

- [1] F. Armero, J.C. Simo, A priori stability estimate and unconditionally stable product formula algorithm for nonlinear coupled thermoplasticity, *Int. J. Plast.* 9 (1993) 749–782.
- [2] T. Antoun, L. Seaman, D.R. Curran, G.I. Kane, S.V. Razorenov, A.V. Utkin, *Spall Fracture*, Springer, New York, 2003.
- [3] T. Belytschko, Y.Y. Lu, L. Gu, Element-free Galerkin methods for static and dynamic fracture, *Int. J. Solids Struct.* 32 (1995) 2547–2570.
- [4] T. Belytschko, Y.Y. Lu, L. Gu, Crack propagation by element-free Galerkin methods, *Engrg. Fract. Mech.* 51 (1995) 295–315.

- [5] J.D. Clayton, Modeling dynamic plasticity and spall fracture in high density polycrystalline alloys, *Int. J. Solids Struct.* 42 (2005) 4613–4640.
- [6] L. Davison, A.L. Stevens, M.E. Kipp, Theory of spall damage accumulation in ductile metals, *J. Mech. Phys. Solids* 9 (1977) 11–28.
- [7] A. Drogoy, D. Rittel, Determination of the JohnsonCCook Material Parameters Using the SCS Specimen, *Exp. Mech.* 9 (2009) 881–885.
- [8] C.A. Duarte, J.T. Oden, Hp clouds – An hp meshless method, *Numer. Meth. Partial Differ. Equat.* 9 (1996) 673–705.
- [9] V.D. Gluzman, G.I. Kanel, Resistance to deformation and fracture of 35Kh3NM steel under conditions of shock loading, *Strength Mater.* 17 (8) (1985) (Translated from *Problemy Prochnosti* 17(8) 52–57).
- [10] S. Hao, W.K. Liu, Moving particle finite element method with superconvergence: nodal integration formulation and applications, *Comput. Meth. Appl. Mech. Engrg.* 195 (2006) 6059–6072.
- [11] S. Hao, W.K. Liu, C.T. Chang, Computer implementation of damage models by finite element and meshfree methods, *Comput. Meth. Appl. Mech. Engrg.* 187 (2000) 401–440.
- [12] B. Hopkinson, A method of measuring the pressure produced in the detonation of high explosives or by the impact of bullets, *Phil. Trans. R. Soc. Lond. A* 213 (1914) 437–456.
- [13] G.R. Johnson, W.H. Cook, A constitutive model and data for metals subjected to large strains, high strain rates and high temperature, in: *Proceedings of the Seventh International Symposium on Ballistics*, 1983, pp. 1–7.
- [14] G.R. Johnson, W.H. Cook, Fracture characteristics of three metals subjected to various strains, strain rates, temperatures and pressures, *Engrg. Fract.* 21 (1985) 31–48.
- [15] G.I. Kanel, S.V. Razorenov, A. Bogatch, A.V. Utkin, Dennis E. Grady, Simulation of spall fracture of aluminum and magnesium over a wide range of load duration and temperature, *Int. Impact Engrg.* 20 (1997) 467–478.
- [16] G.I. Kanel, Spall Fracture: methodological aspects, mechanisms and governing factors, *Int. J. Fract.* 163 (2010) 173–191.
- [17] A.M. Krivtsov, Y.I. Mescheryakov, Molecular dynamics investigation of spall fracture, *Proceedings of SPIE* 3687 (1999) 205–212.
- [18] W.S. Lee, C.F. Lin, Plastic deformation and fracture behaviour of Ti–6Al–4V alloy loaded with high strain rate under various temperatures, *Mater. Sci. Engrg. A* 6 (1998) 48–59.
- [19] S. Li, B.C. Simonsen, Meshfree simulations of ductile crack propagation, *Int. J. Comput. Meth. Engrg. Sci. Mech.* 6 (2005) 1–19.
- [20] S. Li, D. Qian, W.K. Liu, T. Belytschko, A meshfree contact-detection algorithm, *Comput. Meth. Appl. Mech.* 6 (2001) 3271–3292.
- [21] D.C. Simkins, S. Li, Meshfree simulations of thermo-mechanical ductile fracture, *Comput. Mech.* 38 (2005) 235–249.
- [22] S. Li, W.K. Liu, *Meshfree Particle Method*, Springer-Verlag, Berlin, Germany, 2004.
- [23] W.K. Liu, S. Jun, Reproducing kernel particle method, *Int. J. Numer. Meth. Fluids* 6 (1995) 1081–1106.
- [24] W.K. Liu, S. Hao, T. Belytschko, S. Li, C.T. Chang, Multiple scale meshfree methods for damage fracture and localization, *Comput. Mater. Sci.* 16 (1999) 197–205.
- [25] H.W. Meyer, D.S. Kleponis, Modeling the high strain rate behavior of titanium undergoing ballistic impact and penetration, *Int. J. Impact Engrg.* 6 (2001) 509–521.
- [26] J.J. Monaghan, An introduction to SHP, *Comput. Meth. Appl. Mech. Engrg.* 6 (1988) 247–273.
- [27] D. Peirce, C.F. Shih, A. Needleman, A tangent modulus method for the rate dependent solids, *Comput. Struct.* 18 (1984) 168–173.
- [28] A.M. Rajendran, M.A. Dietsberger, D.J. Grove, A void growth-based failure model to describe spallation, *J. Appl. Phys.* 65 (1989) 1521–1527.
- [29] B. Ren, S. Li, Meshfree simulation of plugging failure in high-speed impacts, *Comput. Struct.* 88 (2010) 909–923.
- [30] B.C. Simonsen, S. Li, Meshfree modeling of ductile fracture, *Int. J. Numer. Meth. Engrg.* 60 (2004) 1425–1450.
- [31] D.C. Simkins, S. Li, Meshfree simulations of ductile failure under thermal-mechanical loads, *Comput. Mech.* 38 (2006) 235–249.
- [32] S. Seo, O. Min, H. Yang, Constitutive equation for Ti–6Al–4V at high temperatures measured using the SHPB technique, *Int. J. Impact Engrg.* 38 (2005) 735–754.
- [33] G. Taylor, H. Quinney, The latent energy remaining in a metal; after cold working, *Proc. R. Soc.* 143 (1934) 307–326.
- [34] W.M. Trott, J.N. Castaneda, J.J. O'Hare, M.D. Knudson, L.C. Chhabildas, M.R. Baer, J.R. Asay, Examination of the mesoscopic scale response of shock compressed heterogeneous materials using a line-imaging velocity interferometer, *Fundamental Issues and Applications of Shock-Wave and High-Strain-Rate Phenomena*, vol. 9, Elsevier, Amsterdam, 2001, pp. 47–645.
- [35] T.J. Vogler, J.D. Clayton, Heterogeneous deformation and spall of an extruded tungsten alloy: plate impact experiments and crystal plasticity modeling, *J. Mech. Phys. Solids* 9 (1993) 297–335.
- [36] T.W. Wright, K.T. Ramesh, Dynamic void nucleation and growth in solids: a self-consistent statistical theory, *J. Mech. Phys. Solids* 9 (2008) 297–335.
- [37] Z.P. Wang, K.Y. Lam, Evolution of microcracks in brittle solids under intense dynamic loading, *J. Appl. Phys.* 9 (1995) 3479–3483.
- [38] Z.P. Wang, Void-containing nonlinear materials subject to high-rate loading, *J. Appl. Phys.* 9 (1997) 7213–7227.